I&EC research
Industrial & Engineering Chemistry Research

Article

pubs.acs.org/IECR

Gypsum Crystallization during Phosphoric Acid Production: Modeling and Experiments Using the Mixed-Solvent-Electrolyte Thermodynamic Model

You Peng,[†,‡] Zhilong Zhu,[†,‡] Richard D. Braatz,[†] and Allan S. Myerson*[,†]

[†]Department of Chemical Engineering, Massachusetts Institute of Technology, Cambridge, Massachusetts 02139, United States

Supporting Information

ABSTRACT: The size distributions of calcium sulfate dihydrate crystals formed during the industrial phosphoric acid production process are critical to the acid filtration efficiency. In this work, a thermodynamically consistent definition of supersaturation is derived and modeled using the mixed-solvent-electrolyte framework in *OLI* software for gypsum in an acid mixture. Continuous reactive crystallization experiments are carried out to estimate the gypsum growth and nucleation kinetics at different temperatures. A population balance model is implemented using the method of characteristics and integrated with the thermodynamic model platform to accurately simulate the dynamic propagation of the solution concentration and particle size distribution. The experimentally fitted kinetic parameters are verified through a comparison with the predicted crystal size distribution (CSD) and supersaturation. The comparison shows a good agreement between the predicted and measured CSD and supersaturation at a temperature range from 25 to 60 °C.

INTRODUCTION

About 90% of the world's phosphate consumption goes directly into the fertilizer industry,[1] which is typically accomplished through conversion of the raw phosphate rock to phosphoric acid. Industrial phosphoric acid production makes use of the "wet process", which consists of two steps: (1) sulfuric acid attack of the ores and (2) separation of the acid from the calcium sulfate hydrate crystals produced as a side product.[1] The main reaction involved with calcium phosphate dibasic can be written as[2]

$$CaHPO_4 + H_2SO_4 \xrightarrow{H_2O} H_3PO_4 + CaSO_4 \cdot xH_2O\downarrow$$

where x equals 0, 0.5, or 2 depending on the temperature and acid concentration (see Figure 1).[3] A number of different wet manufacturing processes have been developed in the past that can be summarized into two main categories: the dihydrate process (x = 2, gypsum as the final crystal form) and the nondihydrate process (also known as the hemihydrate process because hemihydrate is involved, although it is not necessarily the final crystal form). The dihydrate process is the earliest developed industrial phosphoric acid production technology. Despite its drawbacks, which include relatively low acid concentration (28−30% P_2O_5) and higher downstream energy consumption, the advantages such as no phosphate rock quality requirement, low operating temperature, infrequent maintenance, simple startup and shutdown operation, and easy scalability still make the dihydrate process the most widely used technique.[1] Immediately after the reactive crystallization step, filtration is carried out to separate acid from gypsum crystals. The overall productivity is closely correlated to the efficiency of the filtration step, which highly depends on the crystal shape and size distributions.

Past studies on gypsum (or hemihydrate) crystallization in phosphoric acid solutions usually involve the study of crystal growth and nucleation kinetics.[2,4] However, none of these works has used a correct definition of supersaturation when fitting experimental data to obtain kinetic parameters. The high concentration in this multicomponent electrolyte system containing ions and hydrate crystals implies that using the total calcium or calcium sulfate concentration is inappropriate. A formal definition for supersaturation needs to be applied, and

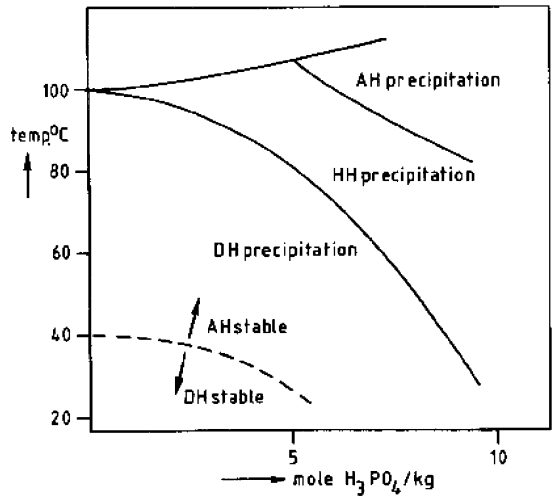

Figure 1. $CaSO_4$ hydrate precipitating as a function of the H_3PO_4 concentration and temperature of the solution. DH: dihydrate, x = 2. HH: hemihydrate, x = 0.5. AH: anhydrite, x = 0. Reprinted with permission from ref 3. Copyright Elsevier 1986.

Received: May 12, 2015
Revised: July 22, 2015
Accepted: July 28, 2015
Published: July 28, 2015

DOI: 10.1021/acs.iecr.5b01763
Ind. Eng. Chem. Res. 2015, 54, 7914−7924

the most intuitive and fundamentally correct way is to follow the thermodynamics, that is, make use of the solubility product ratio, which requires calculation of the activity coefficients as well as free-ion concentrations. These calculations can be achieved by developing a proper model that is capable of performing speciation analysis for the system. For this purpose, this work employs a commercially available software platform with a well-established thermodynamic framework specifically targeted at electrolyte solutions.

Experimental studies were carried out using a mixed-suspension, mixed-product removal (MSMPR) reactive crystallizer. Continuous reactive crystallization experiments were carried out until steady state was achieved at different operating conditions to acquire both the temperature and supersaturation dependency of the crystallization kinetics. An overall population balance model (PBM) used to describe the particle size distribution in a reaction system is implemented and linked to the thermodynamic model, which is built within the *OLI* software platform. Using the fitted kinetic parameters as input to this PBM, crystal size distributions (CSDs) are predicted and verified against experimental measurements from nonseeded MSMPR reactive crystallization.

This work provides a foundation for future study, particularly in the aspect of understanding the effects of impurities on crystal growth and nucleation kinetics. This understanding is needed for completion of the overall model of the acid production process and prediction of the final crystal shape and size distributions, which is essential to perform process optimization to increase acid throughput and minimize liquid waste from entrainment during filtration.

CHEMICAL EQUILIBRIUM MODELING

Gypsum Solubility. Gypsum dissociates in the presence of aqueous solution, and its solubility is governed by solid−liquid equilibrium with its dissociated ions and water molecules. Predicting the gypsum solubility in the concentrated multicomponent electrolyte systems usually encountered in industrial processes can be challenging. Modeling electrolytes assuming complete dissociation can give comparable results for most simple dilute electrolyte systems, but this approach cannot handle the complicated solution chemistry in multicomponent electrolyte systems. To reflect the actual solution chemistry, a speciation-based model is necessary to take into account the chemical equilibria of all species including ionic, metal−ligand complexes and undissociated species.[5] Through speciation analysis, the gypsum solubility can be computed by solving systems of nonlinear equations constrained by the chemical equilibria. The equilibrium constants can be evaluated from the standard-state thermodynamic model.

For concentrated electrolyte systems, the ideal solution assumption is no longer valid because of strong interactions between various species. Modeling of the solution's nonideality has been widely studied, and reviews on these models are available.[6,7] Many of the earlier published models can predict nonideal behavior only up to a certain level of concentration. More recent development of thermodynamic models including the mixed-solvent-electrolyte (MSE) model[8] and the electrolyte nonrandom two-liquid model[9] can account for solution nonideality for the entire concentration range from a pure solvent to a fused salt. It is important to distinguish the concept of speciation from nonideality. A model based on the complete dissociation assumption can still represent nonideal behavior. The MSE model[8] is a speciation-based model that has demonstrated accurate solubility prediction for gypsum systems[10−12] and many other electrolyte chemical systems.[13] This study makes use of the MSE model, which is available in the *OLI* software package, to account for the solution nonideality in characterizing the gypsum solubility.

MSE Model. The standard-state computation in the MSE model relies on the Helgeson−Kirkham−Flowers (HKF)[14] model framework. In this framework, the standard-state Gibbs energy (G°) and any other partial molar properties are modeled based on seven HKF parameters (ω, c_1, c_2, a_1, a_2, a_3, and a_4) as in

$$G^\circ = f(T, P; \omega, c_1, c_2, a_1, a_2, a_3, a_4) \tag{1}$$

where T is the temperature and P is the pressure. When the standard-state Gibbs energy is known for all participating species in any equilibrium reaction (i.e., $aA + bB \leftrightarrows cC + dD$), the equilibrium constant (K_{eq}) can be determined at any given temperature and pressure:

$$K_{eq} = \exp(-\Delta G^\circ/RT) \tag{2}$$

$$\Delta G^\circ = \sum_i \nu_i G_i^\circ \tag{3}$$

where R is the gas constant and ν_i is the stoichiometric coefficient for species i.

The excess Gibbs energy, which describes the solution's nonideality, is modeled based on a combined framework of Debye−Hückel, Bromley, Pitzer, Zemaitis, and other contributors.[15] Typically, the nonideality of an electrolyte solution arises from various forces including the electrostatic (long-range), chemical, and physical dispersion forces.[15] While the electrostatic force is generally valid in dilute solutions, the latter two forces become dominant in concentrated solutions. In order to account for all of these contributions, the excess Gibbs energy in the MSE model is calculated from

$$G^{ex} = G^{ex}_{LR} + G^{ex}_{II} + G^{ex}_{SR} \tag{4}$$

where G^{ex}_{LR} represents the contribution of long-range electrostatic interactions, G^{ex}_{II} accounts for specific ionic (ion−ion and ion−molecule) interactions, and G^{ex}_{SR} is the short-range contribution resulting from intermolecular interactions. The long-range interaction contribution is calculated from the Pitzer−Debye−Hückel formula[16] expressed in terms of mole fractions and is symmetrically normalized. The short-range contribution G^{ex}_{SR} is calculated from the UNIQUAC equation.[17] The specific ion-interaction contribution is calculated from an ionic-strength-dependent, symmetrical second virial coefficient type expression:[15]

$$G^{ex}_{II} = -RT \sum_i n_i \sum_i \sum_j x_i x_j B_{ij}(I_x) \tag{5}$$

where n_i is the number of moles of species i, x_i is the mole fraction of species i, B_{ij} is a binary interaction parameter between the species i and j, $B_{ij}(I_x) = B_{ji}(I_x)$, and $B_{ii} = B_{jj} = 0$, and the ionic strength dependence of B_{ij} is given by

$$B_{ij}(I_x) = b_{ij} + c_{ij} \exp(-\sqrt{I_x + 0.01}) \tag{6}$$

where b_{ij} and c_{ij} are adjustable parameters. In general, the parameters b_{ij} and c_{ij} are functions of the temperature with the form

DOI: 10.1021/acs.iecr.5b01763
Ind. Eng. Chem. Res. 2015, 54, 7914−7924

$$b_{ij}(T) = b_{0,ij} + b_{1,ij}T + \frac{b_{2,ij}}{T} + \frac{b_{3,ij}}{T^2} + b_{4,ij}\ln T \quad (7)$$

$$c_{ij}(T) = c_{0,ij} + c_{1,ij}T + \frac{c_{2,ij}}{T} + \frac{c_{3,ij}}{T^2} + c_{4,ij}\ln T \quad (8)$$

where $b_{0-4,ij}$ and $c_{0-4,ij}$ are coefficients for each interaction pair.

The model equations are embedded in the software package by OLI Systems, Inc., together with some of the model parameters. The preexisting data bank within the software platform includes interaction parameters that were obtained through extensive data collection and fitting done by OLI Systems, Inc. By a comparison of the model predictions (with all available parameters taken from this preexisting database) to literature data, possible missing ion−ion and ion−molecule interactions can be identified. The related interaction parameters, as described in eqs 7 and 8, were found through a similar regression study using available literature data such as solubility, heat capacity, and density. A variety of data are used in one single regression to ensure consistency of the model. All model parameters started with an initial value of zero. Sensitivity analysis was performed to select which model parameters to remove from further consideration and which to keep. Their parameter estimation algorithm uses a series of iterations in which parameters that approach low sensitivity are then fixed and then no longer optimized. The parameter estimation algorithm, as implemented in OLI Systems, Inc., fixes model parameters that have a low sensitivity of the model predictions.

Supersaturation. Accurate estimation of the solution supersaturation is critical in the study of crystal growth and nucleation kinetics. The classical definition of supersaturation $\sigma = (c - c_{eq})/c_{eq}$ may not reflect the actual driving force for gypsum precipitation. A thermodynamically more appropriate definition uses the difference in the chemical potential between a supersaturated state and a solid−liquid equilibrium state as σ.[18,19] The general expression for the chemical potential of species i in the liquid phase is

$$\mu_i = \mu_i^\circ + RT\ln a_i \quad (9)$$

where μ_i° is the standard chemical potential of species i and a_i is the activity of species i, which is a product of its concentration c_i and activity coefficient γ_i. The theoretical dimensionless driving force for crystallization in the liquid phase is

$$\frac{\mu - \mu_{eq}}{RT} = \ln\left(\frac{\prod_{i=1} a_i^{\nu_i}}{\prod_{i=1} a_{i,eq}^{\nu_i}}\right) = \ln\left(\frac{\prod_{i=1} a_i^{\nu_i}}{K_{sp}}\right) \quad (10)$$

where $\mu = \sum \nu_i \mu_i$ and K_{sp} is the solubility product defined as the product of species activity at the solid−liquid equilibrium. The relative supersaturation can be defined as

$$\sigma = \ln S = \ln\left(\frac{\prod_{i=1} a_i^{\nu_i}}{K_{sp}}\right) \quad (11)$$

where the supersaturation ratio S is the ratio between the product of activity and the solubility product. This definition has been used in the evaluation of the potassium chloride crystal growth rate.[20] The σ defined in eq11 is also known as the *growth affinity* in some literature.[21,22] A per unit ion basis has also been seen in some literature to define the supersaturation ratio S' as in[23,24]

$$S' = S^{1/(\nu^+ + \nu^-)} \quad (12)$$

where ν^+ and ν^- are stoichiometric coefficients of the positive and negative species. Another supersaturation expression includes the $\ln S \approx S - 1$ approximation, which is only valid at low supersaturation. The literature continues to use the approximate form of the supersaturation because it resembles the classical form of supersaturation found in the Burton−Cabera−Frank model[25] for crystal growth. In this study, the gypsum supersaturation ratio (S) and relative supersaturation (σ) are defined as

$$S = \frac{a_{SO_4^{2-}} a_{Ca^{2+}} a_{H_2O}^2}{K_{sp,gypsum}} \quad (13)$$

$$\sigma = \ln S \quad (14)$$

The key in estimating the supersaturation in gypsum crystallization or precipitation in general is to have a model that can accurately predict the activity coefficients as well as the free-ion concentration, which has often been neglected in previous studies[4,26] because of the complexity of its evaluation. The activity coefficient is often treated as a constant, in which case the resulting "supersaturation" depends only on the species' concentration. Thermodynamic models such as the Pitzer model have been used in the estimation of gypsum supersaturation,[21,27] and the Bromley model has been used in the estimation of barium sulfate supersaturation,[28] both of which have application in only a limited concentration range. In this study, the state-of-art MSE model is utilized for calculating the activity coefficients and thus the relative supersaturation in the concentrated multicomponent electrolyte system.

CRYSTAL GROWTH AND NUCLEATION KINETICS

Crystal growth and secondary nucleation kinetics are typically modeled by semiempirical functions of supersaturation and temperature as in

$$G = k_g \sigma^g = k_g' \exp\left(\frac{-E_g}{RT}\right)\sigma^g \quad (15)$$

$$B = k_b \sigma^b \mu_3 \delta(L) = k_b' \exp\left(\frac{-E_b}{RT}\right)\sigma^b \mu_3 \delta(L) \quad (16)$$

$$B = B_0 \delta(L) \quad (17)$$

where k_g and k_b are temperature-dependent reaction constants that follow the Arrhenius form, E_g and E_b are activation energies, the third-order moment μ_3 is proportional to the total crystal volume per unit reaction volume, and $\delta(L)$ is a Dirac delta function indicating that new crystals that are birthed have insignificantly small size. These expressions are used in this work because they have been found to be able to explain most of the experimental data.[29]

The model parameters can be estimated by fitting these semiempirical equations against growth and secondary nucleation rates at different supersaturation and temperature levels. Such pairs of data can be obtained by performing continuous crystallization experiments to reach steady state. Growth rate information can be extracted from the steady-state CSD, while the corresponding secondary nucleation rate can be calculated from the overall mass balance, as detailed in the next section.

DOI: 10.1021/acs.iecr.5b01763
Ind. Eng. Chem. Res. 2015, 54, 7914−7924

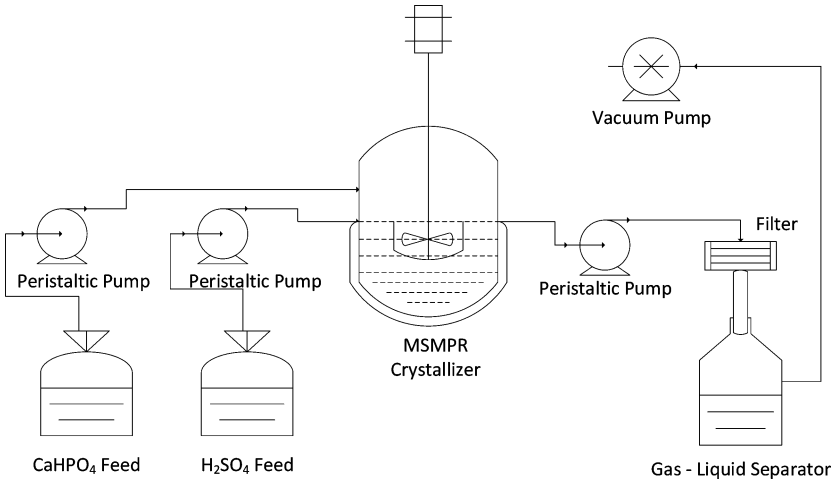

Figure 2. Schematic diagram of the MSMPR experimental setup.

PBM

The PBM[30,31] is the conservation equation for the number of particles. The mathematical framework enables the modeling of particle formation, growth, breakage, and aggregation. PBMs are widely used to model crystallization processes.

Model Equations. The one-dimensional (1D) dynamic population balance equation (PBE) for a continuous crystallization process can be written as

$$\frac{\partial f(L,t)}{\partial t} + G(\sigma)\frac{\partial f(L,t)}{\partial L} = -\frac{f(L,t)}{\tau} \tag{18}$$

where $f(L,t)$ is the crystal number density distribution or number pdf, t is time, L is the crystal size, and τ is the mean residence time of the reactor system. The PBE (18) can be solved for an initial condition given by the CSD of the seed crystals, $f(L,0) = f_{seed}$, and a boundary condition, $f(0,t) = B_0/G$. The assumptions made to arrive at the PBE (18) are as follows: inlet streams contain no particles, reactants are well-mixed in the crystallizer, the reaction volume remains constant, growth is size-independent, and nucleation and growth are dominant kinetic phenomena. The assumption of size-independent growth has been experimentally observed to be true for most, but not all, crystallization systems. Uniform mixing can be easily achieved for small-scale bench experiments.

Because both the growth and secondary nucleation rates depend on supersaturation, which correlates directly with the reactant concentration, the PBE must be solved together with its coupled mass balance equation:

$$\frac{dc_i}{dt} = \nu_i \rho k_v 3G \int_0^\infty fL^2\, dL + \frac{c_{in,i} - c_i}{\tau} \tag{19}$$

where c_i is the concentration of species i in the crystallizer and outlet stream, ν_i is the stoichiometric coefficient of the reaction, c_{in} is the inlet/feed concentration, ρ is the crystal solid density, and k_v is the crystal volume shape factor.

For our system, reactive crystallization takes place with two inlet streams. To handle this situation with PBM, the reaction time is assumed to be instantaneous, which is equivalent to feeding one highly supersaturated calcium sulfate solution.

The steady-state analytical solution for the continuous process is[31]

$$f_{ss}(L) = \frac{B_0}{G}\exp\left(-\frac{L}{G\tau}\right) \tag{20}$$

$$c_{in} - c = M_t \tag{21}$$

$$M_t = \rho k_v \mu_3 = 6\rho k_v \frac{B_0}{G}(G\tau)^4 \tag{22}$$

These equations are used to estimate kinetics.

Numerical Solution: The Method of Characteristics (MOC). Several numerical approaches have been reported in the literature for solving PBEs.[32,33] One of the most efficient and accurate numerical methods for solving PBEs is the MOC, which discovers curves along the $L-t$ plane that transform the PBE (18) into ordinary differential equations:

$$\frac{dL_i}{dt} = G_i \tag{23}$$

$$\frac{df_i}{dt} = -\frac{f_i}{\tau} \tag{24}$$

$$\mu_k = \int_0^\infty fL^k\, dL \approx \sum_i^N f_i L_i^k \Delta L_i \tag{25}$$

where the continuous size domain is evaluated at discrete points L_i, the population density is evaluated at these points referred to as f_i, and the integral term in eq 25 was approximated by a summation. The solution to this system of ODEs gives the characteristic curves that propagate the size density information, which are used to construct the population density function at any given time. In the presence of nucleation, new characteristics are defined to account for the newborn nuclei. The boundary condition is imposed iteratively (every Δt), and the system of ODEs is solved simultaneously using *ode15s* in *Matlab*.

Integration with *OLI* Software. The functionality of the *OLI* software is made possible in other programming environments by OLI Engine 8.2, which is a collection of libraries that enables access to the OLI equilibrium calculation. Access to the OLI functionality was implemented in an Excel Macro based on an example file provided by the OLI Systems, Inc. Because the MOC is solved in the *Matlab* environment, these Excel Macros were used as intermediates that pass the liquid-phase composition from the *Matlab* program to the OLI

DOI: 10.1021/acs.iecr.5b01763
Ind. Eng. Chem. Res. 2015, 54, 7914−7924

Engine. Once a calculation is triggered, the OLI Engine returns speciation and the supersaturation value back to the *Matlab* program. To reduce the number of OLI Engine function calls, the equilibrium computation is only triggered when there is a significant (0.1%) change in the amount of gypsum crystallized.

EXPERIMENTAL SECTION

Materials. For all experiments, reagent-grade calcium phosphate dibasic $CaHPO_4$, sulfuric acid H_2SO_4 (96 wt %), and phosphoric acid H_3PO_4 (85 wt %, 99.99% trace metal basis) were purchased from Sigma-Aldrich. Ultrapure water was used for solvent dilution. A couple of choices such as $CaHPO_4$[34,35] and $Ca(H_2PO_4)_2$[3,36] can be used to model the raw phosphate rock, and the choice should not affect the kinetic results.

Continuous Crystallization Experiments. Figure 2 is a schematic diagram of the experimental setup designed to simulate the wet phosphoric acid production process. Two feed streams consisting of calcium phosphate dibasic and sulfuric acid were pumped continuously into a 50-mL glass-jacketed crystallizer. Overhead mechanical agitation was used to ensure good mixing of the reactants, and the reaction volume was maintained at a constant value by fixing the outlet position. Both inlet solutions were prepared using a diluted phosphoric acid solution (25 wt % P_2O_5) to match the industrial process condition. The detailed feed compositions can be found in Table 1.

Table 1. Feed Compositions (wt %) for All MSMPR Experiments

	$CaHPO_4$	H_2SO_4	P_2O_5
$CaHPO_4$ feed	5.60		23.60
H_2SO_4 feed		4.10	23.98

This MSMPR setup was used to perform reactive crystallization until steady state was achieved. Both feed solutions and the crystallizer were preheated beforehand to the desired temperature and maintained at the same value throughout the experiment. The crystallizer was thermostatically regulated by circulating water through the jacketed walls. The two inlet solutions were fed to an initially empty crystallizer at constant and equal volumetric flow rates. Slurry solutions withdrawn from the outlet were separated into solid and liquid phases by filtration. Here an intermittent withdrawal scheme is employed to remove all of the slurry above the set level (usually around 10% of the total reaction volume); therefore, the withdrawal would take place every 1.5−4.5 min depending on the inlet flow rates, and the discharge time is set to about 25 s. In this way, the outflow rate would be sufficiently high to carry out all crystals and no slurry would settle back to the reactor vessel. Both the particle size distribution and solute concentration were monitored from startup to steady-state operation. Different steady states can be achieved by manipulating the residence time of the reaction system through adjustment of the flow rate of the feed solutions.

Sample Characterization. The system is said to have reached its steady state when (1) the crystal size density reaches a stable distribution and (2) the solute concentration does not change with time. CSD is monitored directly online using focused-beam reflectance measurement (FBRM). Once the particle density was observed to be relatively stable, the solute concentration (total calcium concentration) was then measured using an ion-specific electrode (ISE) from a 100 times diluted sample. The concentration measurement process is repeated every 10−15 min until less than a 1% change is observed for two consecutive measurements. The ISE is only used to further confirm that the system has reached its steady state in addition to a fixed particle density detected by FBRM. Each steady-state liquid sample is analyzed by inductively coupled plasma (ICP) for accurate total calcium, sulfur, and phosphorus element concentrations. All three element concentrations are collected to cross-verify the measurement through the overall mass balance. The steady-state supersaturation ratio defined in eq 13 can then be computed using the MSE thermodynamic model by providing the ICP measured solution composition.

DYNAMIC SIMULATION

To simulate the evolution of the 1D CSD of gypsum crystals in the MSMPR setup, the PBM is solved numerically using the MOC, together with the MSE model for supersaturation evaluation. The systems of ODEs (24) and (25) derived from the PBE (18) and the differential mass balance (19) for each species were solved simultaneously using *ode15s* in *Matlab*. The parameters associated with the growth and secondary nucleation model determined in this study, as reported in the Results and Discussion section, are used in the simulations. The simulation conditions including temperature, residence time, initial concentration, and feed concentration are based on the experimental conditions, as specified in Table 2 and in the Results and Discussion section. The concentration conversion from weight fraction in Table 1 to molarity in Table 2 was based on the solution density computed by the *OLI* software, which is consistent with the measured density of 1.26 g/mL at 25 °C. For convenience, P_2O_5 was converted to an equivalent amount of H_3PO_4 and H_2O.

Table 2. Feed and Initial Concentrations of All Species in the Dynamic Simulation at 25 °C

species	ν	c_{in} (M)	c_0 (M)
$CaSO_4{\cdot}2H_2O$	+1	0	0.001
$CaHPO_4$	−1	0.259	0.259
H_2SO_4	−1	0.263	0.263
H_2O	−2	43.6	43.6
H_3PO_4	+1	4.22	4.22

To begin the simulation, a small amount of seed crystals was introduced to initiate secondary nucleation. In reality, primary nucleation will generate the initial crystal that we artificially introduced. The seed crystals that we introduced will diminish and will not affect the steady-state CSD. The initial concentration in the solution (c_0) is set to have the same concentration as the feed solution. Other parameters defined in the simulation are available in the Supporting Information.

RESULTS AND DISCUSSION

Thermodynamic Model. Initial analysis on the preloaded OLI data bank (MSEPUB data bank) showed that some of the critical interaction parameters of this multicomponent system (gypsum in acid mixtures) had already been derived because of the fact that a variety of the subsystems (the related binary and ternary systems) had already been studied in the past (Table 3) by OLI Systems, Inc. This past work is very important because the additive principle of the MSE model enables property prediction of complex multicomponent systems using param-

DOI: 10.1021/acs.iecr.5b01763
Ind. Eng. Chem. Res. 2015, 54, 7914−7924

Table 3. Subsystems of $CaSO_4$–H_3PO_4–H_2SO_4–H_2O Studied by OLI Systems, Inc.

subsystem	CaO	$CaSO_4$	H_3PO_4	H_2SO_4	H_2O
1		√			√
2				√	√
3			√		√
4	√		√		√

eters obtained from the studies of subsystems. Therefore, part of the main interaction parameters related to our system were already in the OLI data bank, and only the missing parameters needed to be identified and estimated.

Further observation indicated that the only missing interactions were between the phosphate- and sulfate-related species (ions or molecules). Detailed speciation analysis was performed using the *OLI* software, and the most abundant species in this multicomponent system were identified to be H_3PO_4, $H_2PO_4^-$, H_3O^+, P_2O_5, HSO_4^-, and $CaSO_4$. The interaction parameters between these most abundant species, as described in eqs 7 and 8, were estimated through regression analysis. The literature data used for parameter estimation can be found in the Supporting Information. Solubility data of all three $CaSO_4$ hydrate forms were used because they share the exact same set of electrolyte species in solution form, which also ensured consistency and accuracy of the fitted model parameters.

The major fitted interaction parameters included in the model are listed in Table 4. With these fitted model parameters,

Table 4. Major Fitted Interaction Parameters Included in the MSE Model

species i	species j	b_{ij}	c_{ij}
$CaSO_4$	$H_2PO_4^-$	$b_{0,ij} - b_{4,ij}$	$c_{0,ij} - c_{4,ij}$
$CaSO_4$	H_3PO_4	$b_{0,ij} - b_{4,ij}$	$c_{0,ij} - c_{4,ij}$
$CaSO_4$	P_2O_5	$b_{0,ij} - b_{3,ij}$	$c_{0,ij} - c_{3,ij}$
$CaSO_4$	H_3O^+	$b_{0,ij} - b_{4,ij}$	$c_{0,ij} - c_{4,ij}$
H_3PO_4	P_2O_5	$b_{3,ij}$	$c_{3,ij}$
$H_2PO_4^-$	P_2O_5		$c_{3,ij}$

both the calculated and literature experimental values of the gypsum solubility in phosphoric acid solutions and acid mixtures are shown in Figures 3 and 4. Both plots indicate that the model fits the data set well for a wide range of temperatures (25–80 °C) and acid concentrations.

The model was validated through a comparison of its predictions with experimental values[40] of hemihydrate solubility in phosphoric acid solutions at 90 °C. Results are plotted in Figure 5. It is clear from the verification plot that the MSE model predicts accurately the solubility of hemihydrate in the phosphoric acid solution using the fitted interaction parameters at an extrapolated temperature (90 °C), which also demonstrates its ability to handle a wide range of temperature and acid compositions. This model was then used throughout the study for computation of supersaturation at any given conditions.

Kinetics. The kinetic parameters of the semiempirical growth and nucleation relations (15) and (16) were estimated using data collected from steady-state MSMPR experiments. Equations 15 and 16 were transformed by taking the logarithm at both sides so that linear regression can be applied. The growth rate exponent was fixed at 2, while all of the other

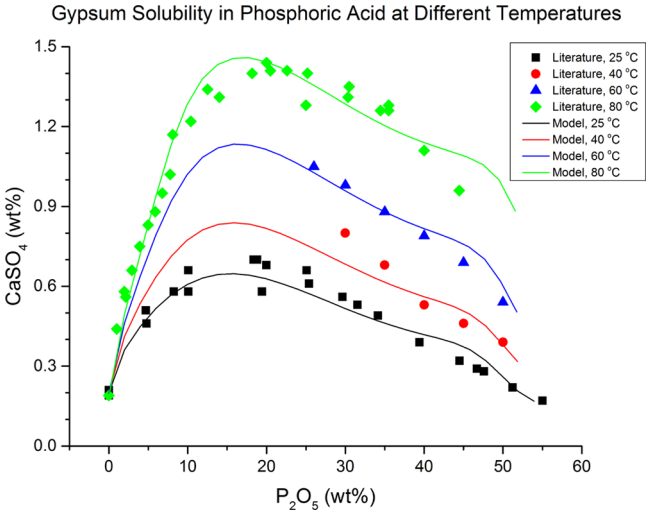

Figure 3. $CaSO_4 \cdot 2H_2O$ solubility as a function of the phosphoric acid concentration at different temperatures. Points are literature experimental data.[37,38] Curves are OLI model calculations.

kinetic parameters were fitted. The detailed experimental conditions of all of the MSMPR experiments conducted were summarized in Table 5. The model parameters were fit for the 25, 40, and 60 °C data. The estimated growth and nucleation kinetic parameters are summarized in Table 6.

The model-calculated growth and nucleation rates and the experimentally measured values at different supersaturations as well as temperatures are plotted against each other in Figures 6 and 7. The power law relation with an Arrhenius form of the rate constant is observed to well describe the gypsum crystal growth rate in phosphoric acid solutions. The nucleation rate is found to have a very weak dependence on the temperature (the hypothesis test of $E_b/R = 0$ gives a P value of 0.4, which indicates that it is not necessary to include the temperature term in the model); therefore, a fixed rate constant is used in the rate law instead of the Arrhenius form. Efforts were made to compare our numbers with the previously published results; however, a very limited study on the kinetics of gypsum crystallization from a phosphoric acid solution has been found (most of the literature work involves a different solution system such as water, salt water, or sulfuric acid). The only prior result that we could find that studies the exact same system is from White,[2] where the presented growth rate also employs an Arrhenius-form rate constant with a second-order supersaturation dependency and the nucleation rate has no temperature term with only a first-order supersaturation dependency. However, their study defines supersaturation in terms of the concentration of the total calcium ion, which is not a proper way to represent supersaturation as pointed out in this paper. A numerical comparison has been made between our and their kinetic models at the same conditions. The growth rate prediction is about 30–60 times different, while the nucleation rate prediction is different by orders of magnitude. Overall, it seems that there are not any previously published results that are directly comparable to the results presented here.

Again, model verification is performed using the last set of data collected from the MSMPR experiments at 50 °C, with results shown in Figures 8 and 9. The predicted growth and nucleation rates are reasonably consistent with the experimental data.

DOI: 10.1021/acs.iecr.5b01763
Ind. Eng. Chem. Res. 2015, 54, 7914–7924

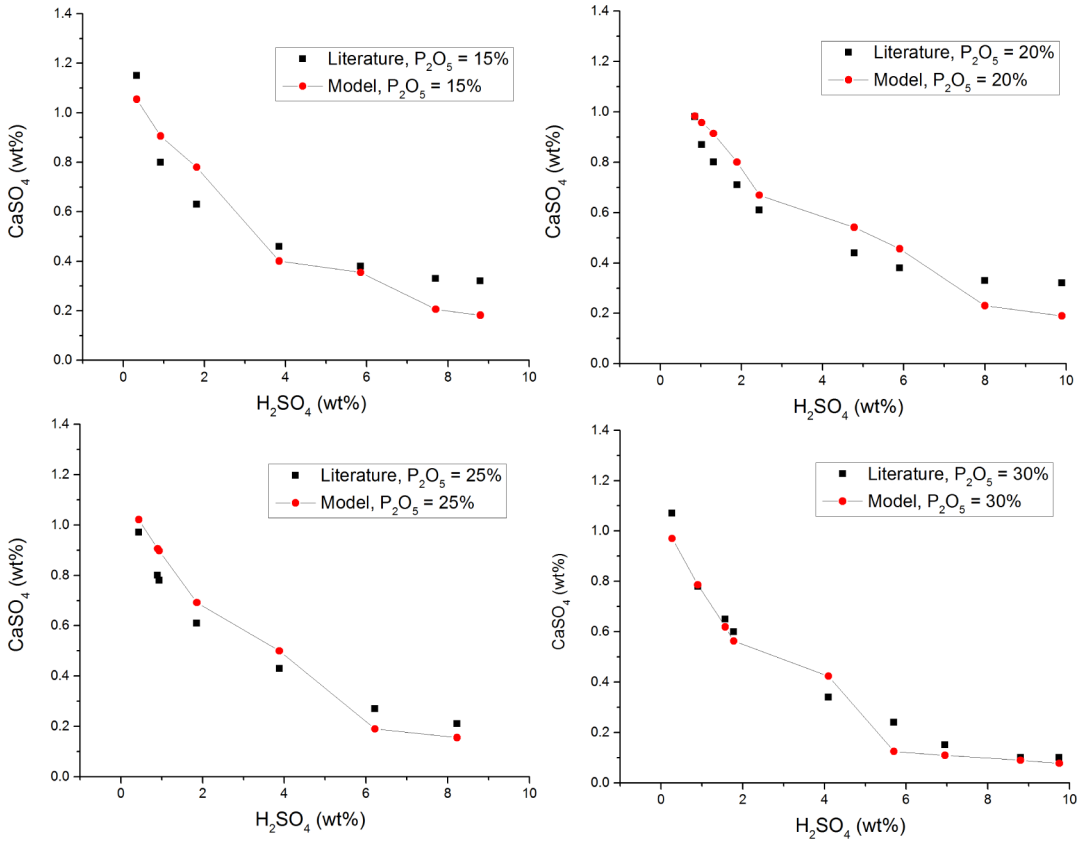

Figure 4. $CaSO_4 \cdot 2H_2O$ solubility as a function of the sulfuric acid concentration at 70 °C. Black points are literature experimental data.[39] Red points are OLI model calculations, with lines between the points used only to direct the eye.

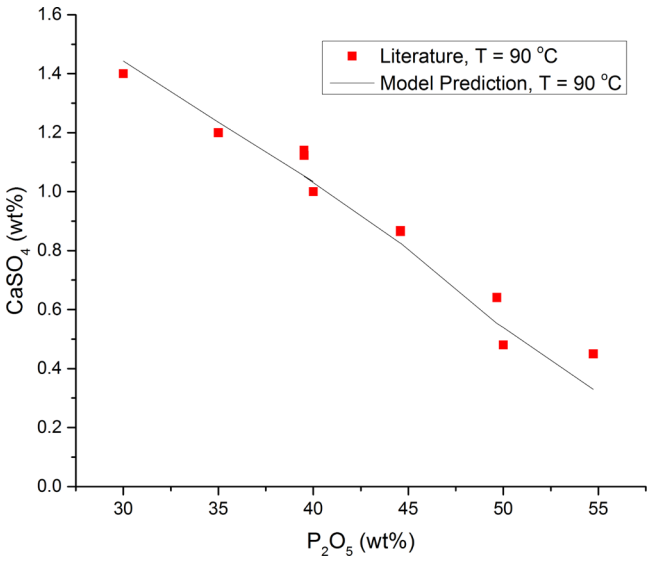

Figure 5. $CaSO_4 \cdot 0.5H_2O$ solubility as a function of the phosphoric acid concentration at 90 °C. Red points are literature experimental data.[40] The black line is the OLI model prediction.

Simulation Results. The simulated CSD and supersaturation at steady state correspond well with those measured at four different temperatures, as shown in Figure 10 and Table 7. To compare the simulated and measured CSD on the same basis, the CSD from simulation and experiments were converted from a number pdf (f) to a normalized volume pdf (f_{vol}) as in

Table 5. Experimental Conditions for MSMPR Experiments

expt. no.	temperature (°C)	residence time (min)	feed flow rate (mL/min)	agitation rate (rpm)
1–3	25	12, 24, 54	1.70, 0.90, 0.40	350
4–6	40	24, 32, 75	1.40, 1.00, 0.45	350
7–9	60	17, 30, 64	1.50, 0.85, 0.50	350
10–12	50	19, 23, 55	1.10, 0.90, 0.40	350

Table 6. Fitted Growth and Nucleation Kinetic Parameters

parameters	G	parameters	B
ln k_g' (μm/min)	28.449 ± 3%	ln k_b' (#/m^3·min)	27.363 ± 0.5%
E_g/R (K)	8.53× 10^3 ± 3%	E_b/R (K)	
g	2.00	b	2.88 ± 5%

$$f_{vol,i} = \frac{f_i L_i^3}{\sum_{i=1}^{N} f_i L_i^3 \Delta L_i} \tag{26}$$

where $\Delta L_i = L_{i+1} - L_i$.

Figure 11 plots the dynamic evolution of the volume-normalized CSD from the model simulation for the experimental conditions at 40 °C and τ = 32 min. The evolution shows the disappearance of the seeded crystals and the growth of the newborn crystals that reach steady-state CSD after about 300 min. The corresponding supersaturation ratio profile and solids concentration profile for the simulation are shown in Figure 12. Initially, the solution supersaturation is high, but the rate of change in the crystal mass remains low because we only introduce a small amount of seeded crystals to initiate secondary nucleation. At this point, newborn crystals

DOI: 10.1021/acs.iecr.5b01763
Ind. Eng. Chem. Res. 2015, 54, 7914–7924

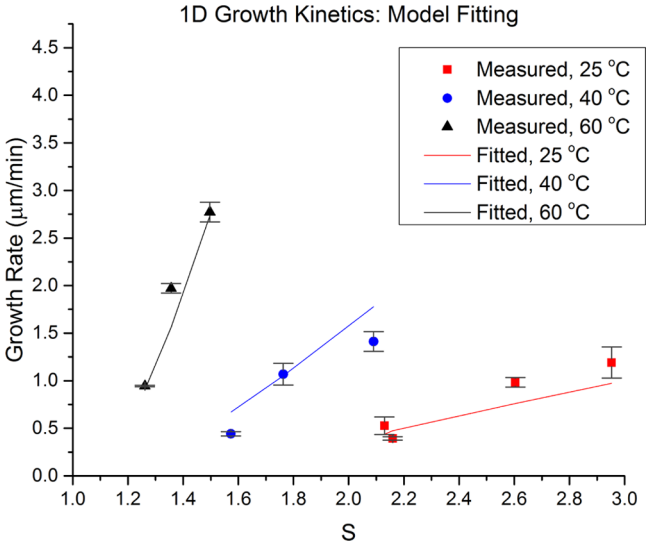

Figure 6. $CaSO_4 \cdot 2H_2O$ 1D growth kinetics at different supersaturation ratios and temperatures. Points are experimental measurements. The lines are the power law model calculation.

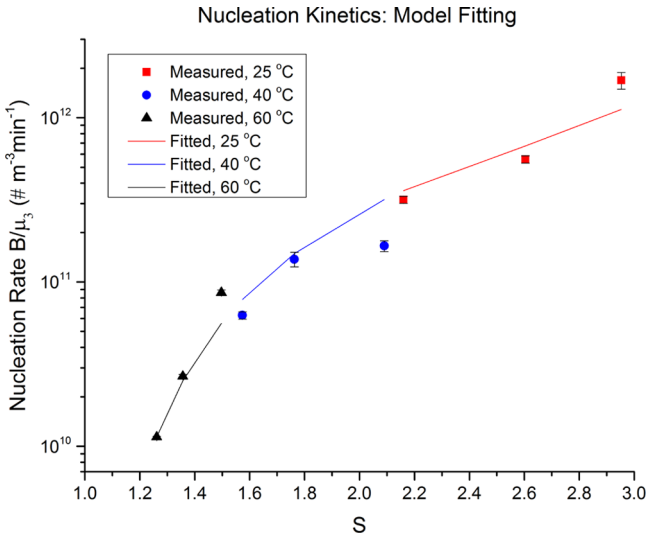

Figure 7. $CaSO_4 \cdot 2H_2O$ secondary nucleation kinetics at different supersaturation ratios and temperatures. Points are experimental measurements. The lines are the power law model calculation.

from secondary nucleation are still too small for growth to have a significant effect on the total mass of crystals. As newborn crystals grow and increase in number, the growth of the newborn crystals dominates and accounts almost entirely for the increase in the total crystal mass and depletion of supersaturation. The large increase in the total crystal mass offsets the initial drop in supersaturation, and as a result, the nucleation rate further increases. At some point, the drop in supersaturation outweighs the increase in the crystal concentration and consequently slows the nucleation rate. The supersaturation reaches a steady state when the consumption rate equilibrates with the replenish rate by the feed solution. It is interesting to note that the time to reach steady state in terms of the supersaturation and overall mass is approximately 150 min (Figure 12), while the time to reach steady state in terms of the CSD (Figure 11) is much longer. The longer response time indicates slower dynamics for the CSD.

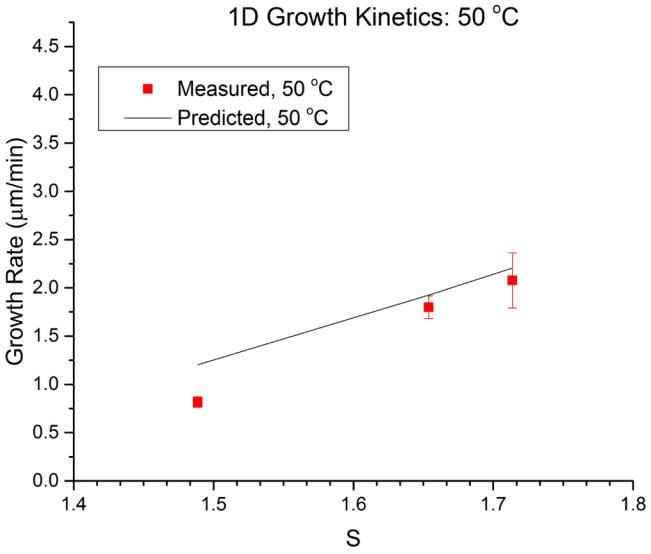

Figure 8. $CaSO_4 \cdot 2H_2O$ 1D growth kinetics at different supersaturation ratios and 50 °C. Points are experimental measurements. The line is the power law model prediction.

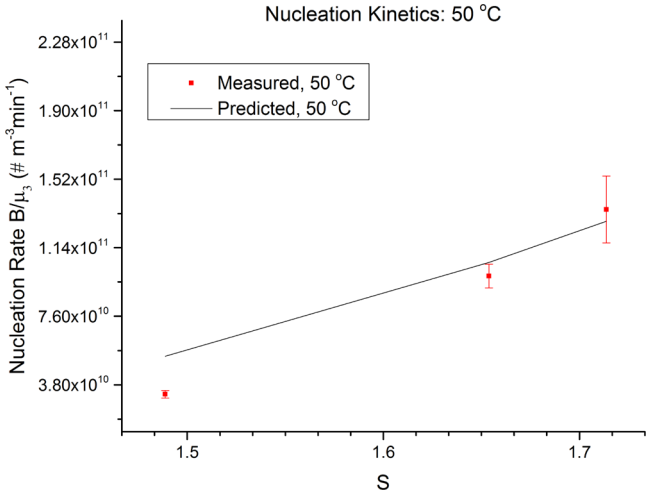

Figure 9. $CaSO_4 \cdot 2H_2O$ secondary nucleation kinetics at different supersaturation ratios and 50 °C. Points are experimental measurements. The line is the power law model prediction.

The dynamic evolution of the CSD in Figure 11 was converted to moments. The first four moments are compared to the numerical solution from the standard method of moments (MOM), as shown in Figure 13. The MOM provides a benchmark for comparing the accuracy of the MOC implemented (Supporting Information). The comparison shows that the MOC implementation is accurate. It is also interesting to note the presence of an overshoot and that the overshoot becomes less obvious for higher moments, as in Figure 13. The overshoot observed in the simulation is a result of a delayed response on the CSD when the nucleation rate reached and passed its maximum value.

CONCLUSION

This article reports the determination and cross-validation of gypsum crystallization kinetics experimentally using a steady-state MSMPR operated at various temperatures and supersaturation. Compared to the previously reported gypsum crystal

DOI: 10.1021/acs.iecr.5b01763
Ind. Eng. Chem. Res. 2015, 54, 7914−7924

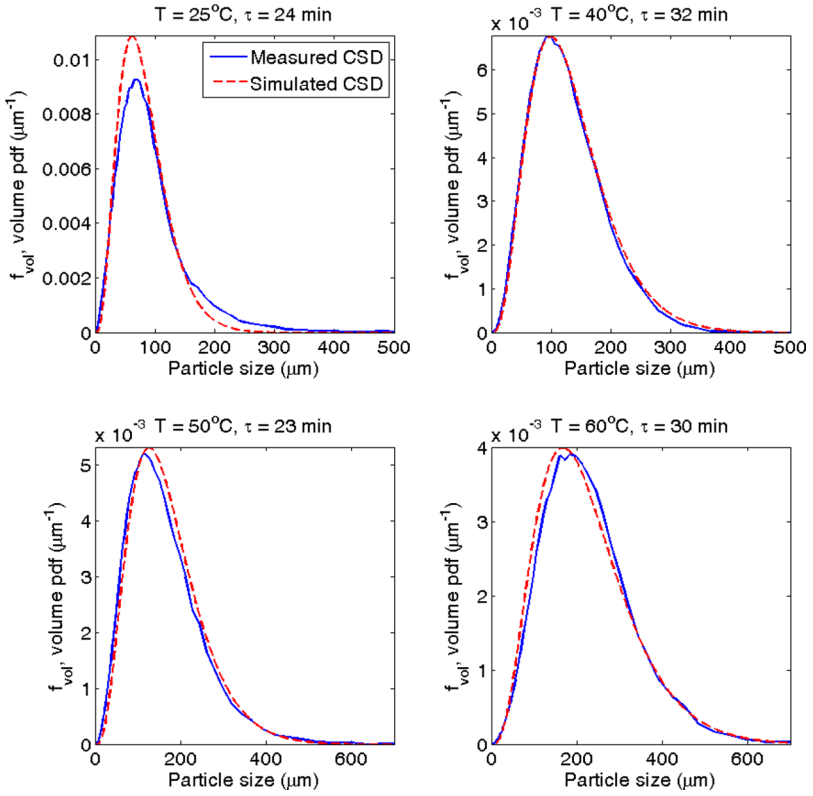

Figure 10. Comparison of the predicted and measured steady-state CSDs at various conditions in Table 7. The measured CSDs were obtained by measuring the crystal slurry using FBRM to give chord length distribution, which was then converted to volume-based CSD.

Table 7. Simulated and Measured Steady-State Supersaturation Ratios at Different Conditions

T (°C)	τ (min)	$S_{measured}$	$S_{predicted}$
25	24	2.60	2.75
40	32	1.76	1.75
50	23	1.65	1.63
60	30	1.36	1.39

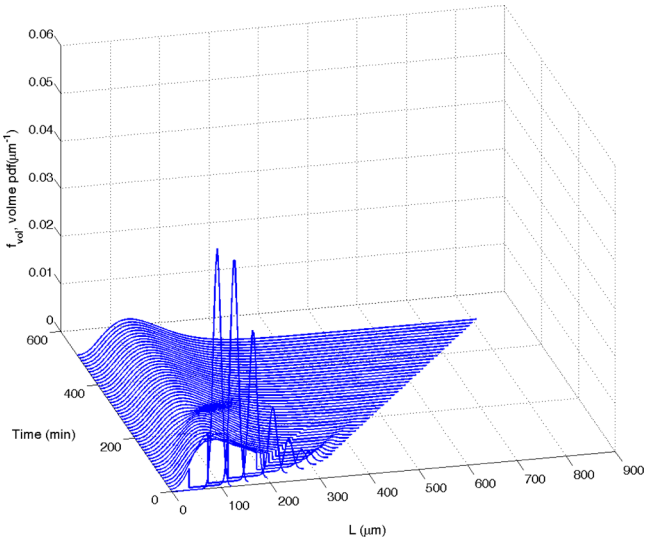

Figure 11. Dynamic evolution of the CSD in the MSMPR model for the experimental conditions at 40 °C and τ = 32 min.

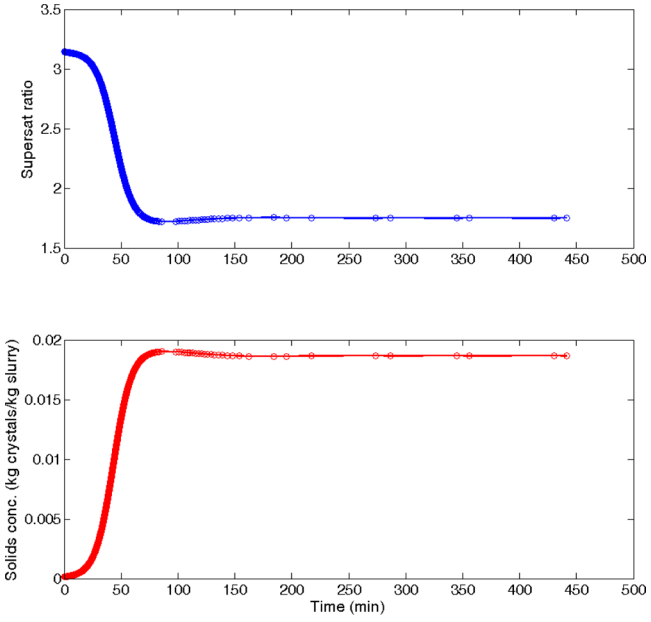

Figure 12. Supersaturation ratio and solids concentration profiles from the dynamic simulation of the MSMPR setup for T = 40 °C and τ = 32 min. The circles represent OLI function calls, which become less frequent as the system reaches steady state.

kinetics literature, this approach employs an accurate supersaturation determined based on the MSE thermodynamic model. The MSE model framework allows the prediction of solution supersaturation for concentrated multicomponent electrolytes found in more complex solution chemistry. To verify the measured gypsum nucleation and growth kinetics, the PBM was solved numerically using the MOC, together with the MSE thermodynamic model. The numerical solution reaches

DOI: 10.1021/acs.iecr.5b01763
Ind. Eng. Chem. Res. 2015, 54, 7914−7924

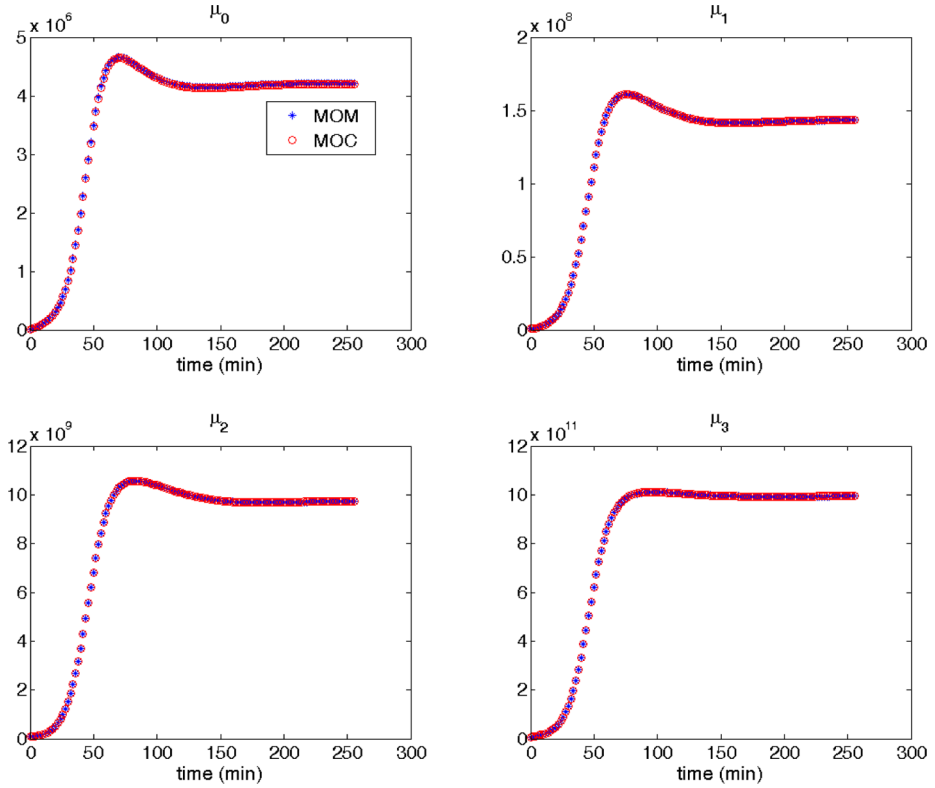

Figure 13. Comparison of the first four moments when solved using MOC and MOM in the dynamic simulation of the MSMPR setup for T = 40 °C and τ = 32 min.

steady state and closely reproduces the measured steady-state CSD and supersaturation at 25, 40, 50, and 60 °C. To the best of our knowledge, this is the first coupling of the MSE model, with the PBM simulating the dynamic evolution of CSD. This integrated model framework provides a foundation for understanding reactive crystallization in more complex solution chemistry such as in the industrial wet process.

■ ASSOCIATED CONTENT

Supporting Information

The Supporting Information is available free of charge on the ACS Publications website at DOI: 10.1021/acs.iecr.5b01763.

Literature solubility data used for MSE model parameter estimation, values of the fitted MSE interaction parameters, specifications in the MSMPR simulation, and model equations for the first four moments (PDF)

■ AUTHOR INFORMATION

Corresponding Author

*Tel.: 617-452-3790. E-mail: myerson@mit.edu.

Author Contributions

‡Coauthors that equally contributed to this work.

Notes

The authors declare no competing financial interest.

■ ACKNOWLEDGMENTS

The authors thank technical advisers from OLI Systems, Inc., for assisting in the data regression and providing example files to access the OLI Engine. This research is funded by the OCP Group.

■ REFERENCES

(1) Becker, P. *Phosphates and Phosphoric Acid: Raw Materials, Technology, and Economics of the Wet Process*, 2nd ed.; Marcel Dekker: New York, 1989.

(2) White, E.; Mukhopadhyay, S. In *Crystallization as a Separations Process*; Myerson, A. S., Toyokura, K., Eds.; American Chemical Society: Washington, DC, 1990; Chapter 23, pp 292−315.

(3) Van Der Sluis, S.; Witkamp, G.; Van Rosmalen, G. Crystallization of Calcium Sulphate in Concentrated Phosphoric Acid. *J. Cryst. Growth* **1986**, *79*, 620−629.

(4) EL Moussaouiti, M.; Boistelle, R.; Bouhaouss, A.; Klein, J. Crystallization of Calcium Sulphate Hemihydrate in Concentrated Phosphoric Acid Solutions. *Chem. Eng. J.* **1997**, *68*, 123−130.

(5) Anderko, A.; Wang, P.; Rafal, M. Electrolyte Solutions: From Thermodynamic and Transport Property Models to the Simulation of Industrial Processes. *Fluid Phase Equilib.* **2002**, *194*, 123−142.

(6) Loehe, J. R.; Donohue, M. D. Recent Advances in Modeling Thermodynamic Properties of Aqueous Strong Electrolyte Systems. *AIChE J.* **1997**, *43*, 180−195.

(7) Lin, Y.; Kate, A. t.; Mooijer, M.; Delgado, J.; Fosbøl, P. L.; Thomsen, K. Comparison of Activity Coefficient Models for Electrolyte Systems. *AIChE J.* **2010**, *56*, 1334−1351.

(8) Wang, P.; Anderko, A.; Young, R. D. A Speciation-based Model for Mixed-Solvent Electrolyte Systems. *Fluid Phase Equilib.* **2002**, *203*, 141−176.

(9) Chen, C.-C.; Song, Y. Generalized Electrolyte-NRTL Model for Mixed-Solvent Electrolyte Systems. *AIChE J.* **2004**, *50*, 1928−1941.

(10) Azimi, G.; Papangelakis, V.; Dutrizac, J. Modelling of Calcium Sulphate Solubility in Concentrated Multi-Component Sulphate Solutions. *Fluid Phase Equilib.* **2007**, *260*, 300−315.

(11) Azimi, G.; Papangelakis, V.; Dutrizac, J. Development of an MSE-Based Chemical Model for the Solubility of Calcium Sulphate in Mixed Chloride-Sulphate Solutions. *Fluid Phase Equilib.* **2008**, *266*, 172−186.

DOI: 10.1021/acs.iecr.5b01763
Ind. Eng. Chem. Res. 2015, 54, 7914−7924

(12) Azimi, G.; Papangelakis, V. Thermodynamic Modeling and Experimental Measurement of Calcium Sulfate in Complex Aqueous Solutions. *Fluid Phase Equilib.* **2010**, *290*, 88−94.
(13) Wang, P.; Anderko, A.; Springer, R.; Young, R. Modeling Phase Equilibria and Speciation in Mixed-Solvent Electrolyte Systems: II. Liquid−Liquid Equilibria and Properties of Associating Electrolyte Solutions. *J. Mol. Liq.* **2006**, *125*, 37−44.
(14) Sandler, S. I. *Models for Thermodynamic and Phase Equilibria Calculations*; Dekker: New York, 1994.
(15) Wang, P.; Anderko, A.; Young, R. A Speciation-Based Model for Mixed-Solvent Electrolyte Systems. *Fluid Phase Equilib.* **2002**, *203*, 141−176.
(16) Pitzer, K. S.; Mayorga, G. Thermodynamics of Electrolytes. II. Activity and Osmostic Coefficients for Strong Electrolytes with One or Both Ions Univalent. *J. Phys. Chem.* **1973**, *77*, 2300−2308.
(17) Abrams, D. S.; Prausnitz, J. M. Statistical Thermodynamics of Liquid Mixtures: A New Expression for the Excess Gibbs Energy of Partly or Completely Miscible Systems. *AIChE J.* **1975**, *21*, 116−128.
(18) Mersmann, A. *Crystallization Technology Handbook*, 2nd ed.; Marcel Dekker: New York, 2001.
(19) Mullin, J.; Söhnel, O. Expressions of Supersaturation in Crystallization Studies. *Chem. Eng. Sci.* **1977**, *32*, 683−686.
(20) Cheng, W.; Bo, Q.; Cheng, F.; Du, Z. Crystal Growth Rate of KCl in the KCl-$MgCl_2$-H_2O System Based on MSE Modeling. *Ind. Eng. Chem. Res.* **2013**, *52*, 17658−17666.
(21) Witkamp, G.; Van der Eerden, J.; Van Rosmalen, G. Growth of Gypsum: I. Kinetics. *J. Cryst. Growth* **1990**, *102*, 281−289.
(22) Guan, B.; Yang, L.; Wu, Z. Effect of Mg^{2+} Ions on the Nucleation Kinetics of Calcium Sulfate in Concentrated Calcium Chloride Solutions. *Ind. Eng. Chem. Res.* **2010**, *49*, 5569−5574.
(23) Yoshikawa, Y.; Nancollas, G.; Barone, J. The Kinetic of Crystallization of Group II Fluoride Salts in Aqueous Solution. *J. Cryst. Growth* **1984**, *69*, 357−361.
(24) Hamdona, S. K.; Al Hadad, U. A. Crystallization of Calcium Sulfate Dihydrate in the Presence of Some Metal Ions. *J. Cryst. Growth* **2007**, *299*, 146−151.
(25) Ohara, M.; Reid, R. C. *Modeling Crystal Growth Rates From Solution*; Prentice Hall: Englewood Cliffs, NJ, 1973.
(26) Liu, S.-T.; Nancollas, G. H. The Kinetics of Crystal Growth of Calcium Sulfate Dihydrate. *J. Cryst. Growth* **1970**, *6*, 281−289.
(27) He, S.; Oddo, J. E.; Tomson, M. B. The Seeded Growth of Calcium Sulfate Dihydrate Crystals in NaCl Solutions up to 6 m and 90 C. *J. Colloid Interface Sci.* **1994**, *163*, 372−378.
(28) Wei, H.; Garside, J. Application of CFD Modelling to Precipitation Systems. *Chem. Eng. Res. Des.* **1997**, *75*, 219−227.
(29) Myerson, A. S. *Handbook of Industrial Crystallization*, 2nd ed.; Butterworth-Heinemann: Woburn, MA, 2002.
(30) Hulburt, H.; Katz, S. Some Problems in Particle Technology: A Statistical Mechanical Formulation. *Chem. Eng. Sci.* **1964**, *19*, 555−574.
(31) Randolph, A. D.; Larson, M. A. *Theory of Particulate Processes: Analysis and Techniques in Continuous Crystallization*, 2nd ed.; Academic Press: San Diego, CA, 1988.
(32) Costa, C. B. B.; Maciel, M. R. W.; Filho, R. M. Considerations on the Crystallization Modeling: Population Balance Solution. *Comput. Chem. Eng.* **2007**, *31*, 206−218.
(33) Alexopoulos, A.; Roussos, A.; Kiparissides, C. Part I: Dynamic Evolution of the Particle Size Distribution in Particulate Processes Undergoing Combined Particle Growth and Aggregation. *Chem. Eng. Sci.* **2004**, *59*, 5751−5769.
(34) Abdel-Aal, E.; Rashad, M.; El-Shall, H. Crystallization of Calcium Sulfate Dihydrate at Different Supersaturation Ratios and Different Free Sulfate Concentration. *Cryst. Res. Technol.* **2004**, *39*, 313−321.
(35) Rashad, M.; Mahmoud, M.; Ibrahim, I.; Abdel-Aal, E. Crystallization of Calcium Sulfate Dihydrate Under Simulated Condition of Phosphoric Acid Production in the Presence of Aluminum and Magnesium Ions. *J. Cryst. Growth* **2004**, *267*, 372−379.
(36) Amin, A. B.; Larson, M. A. Crystallization of Calcium Sulfate from Phosphoric Acid. *Ind. Eng. Chem. Process Des. Dev.* **1968**, *7*, 133−137.
(37) Taperova, A. A. L'Analyse Physicochimique ans Le Domaine Du Traitement Des Phosphates Par L'Acide Sulfurique. *Zh. Prikl. Khim.* **1940**, *13*, 634−651.
(38) Taperova, A. A.; Shulgiva, M. H. Solubilities of $CaSO_4$ Hydrates in Phosphoric Acid. *Zh. Prikl. Khim.* **1945**, *18*, 521−528.
(39) Kurteva, O. I.; Brustkus, E. B. Solubilities of Calcium Sulfate In H_3PO_4 + H_2SO_4 and H_3PO_4 + H_2SiF_6 acid Mixtures. *Zh. Prikl. Khim.* **1961**, *34*, 1714−1722.
(40) Sullivan, J. M.; Kohler, J. J.; Grinstead, J. H., Jr. Solubilities of α-Calcium Sulfate Hemihydrate 40, 45, 50, and 55% P_2O_5 Phosphoric Acid Solutions at 80, 90, 100 and 110 °C. *J. Chem. Eng. Data* **1988**, *33*, 367−370.

DOI: 10.1021/acs.iecr.5b01763
Ind. Eng. Chem. Res. 2015, 54, 7914−7924